

Improved Estimates of Preindustrial Biomass Burning Reduce the Magnitude of Aerosol Climate Forcing in the Southern Hemisphere

Pengfei Liu (1,2)*, Jed O. Kaplan (3), Loretta J. Mickley (1), Yang Li (1), Nathan J. Chellman (4),
Monica M. Arienzo (4), John K. Kodros (5), Jeffrey R. Pierce (5), Michael Sigl (6,7), Johannes Freitag
(8), Robert Mulvaney (9), Mark A. J. Curran (10), and Joseph R. McConnell (4,11)

- (1) School of Engineering and Applied Sciences, Harvard University, Cambridge, MA, 02138, USA
- (2) School of Earth and Atmospheric Sciences, Georgia Institute of Technology, Atlanta, GA, 30332, USA
- (3) Department of Earth Sciences, The University of Hong Kong, Hong Kong, China
- (4) Division of Hydrologic Sciences, Desert Research Institute, NV 89512, USA
- (5) Department of Atmospheric Science, Colorado State University, Fort Collins, Colorado 80523, USA
- (6) Oeschger Centre for Climate Change Research, University of Bern, 3012 Bern, Switzerland
- (7) Climate and Environmental Physics, University of Bern, 3012 Bern, Switzerland
- (8) Alfred-Wegener-Institut Helmholtz-Zentrum für Polar- und Meeresforschung, Bremerhaven, Germany
- (9) British Antarctic Survey, Cambridge, UK
- (10) Australian Antarctic Division and Antarctic Climate and Ecosystem Cooperative Research Centre, Hobart, Tasmania, Australia
- (11) Sir Nicholas Shackleton Visiting Fellow, Clare Hall, University of Cambridge, CB3 9AL Cambridge, United Kingdom

E-mail: pengfei.liu@eas.gatech.edu

To be submitted to:

Science Advances

*To Whom Correspondence Should be Addressed

1 **Abstract**

2 **Fire plays a pivotal role in shaping terrestrial ecosystems and the chemical**
3 **composition of the atmosphere, and thus influences Earth’s climate. The trend and**
4 **magnitude of fire activity over the last few centuries are controversial, which hinders**
5 **understanding of preindustrial to present-day aerosol radiative forcing. Here we present new**
6 **evidence from records of 14 Antarctic ice cores and 1 central Andean ice core, suggesting**
7 **that historical fire activity in the Southern Hemisphere (SH) significantly exceeded present-**
8 **day levels. To understand this observation, we use a global fire model to show that overall**
9 **SH fire emissions could have declined by 30% over the 20th century, possibly because of the**
10 **rapid expansion of land use for agriculture and animal production. Radiative forcing**
11 **calculations suggest that the decreasing trend in SH fire emissions over the last century**
12 **largely compensates for the cooling effect of increasing aerosols from fossil fuel and biofuel**
13 **sources.**

14

15 **Introduction**

16 Both climate variability and human activity drive changes in wildfire frequency and
17 magnitude. During the last millennium, the human imprint on wildfire has become increasingly
18 important because of landscape fragmentation through land use, and more recently through large-
19 scale active fire suppression (1). For the time scale relevant to climate change in the industrial era,
20 a key uncertainty is where and to what extent human activity has altered fire activity (2). As a
21 major source of fire ignition, humans use fire for land clearance, thus introducing fire to areas that
22 are unlikely to burn naturally, such as tropical rainforests or peatlands (3). In contrast, recent
23 analyses have suggested that anthropogenic land cover change and landscape fragmentation

24 significantly reduce fire in savannas by affecting fuel load and fire spread, and the fire activity
25 over human-manged land is lower than that in natural conditions (4-6). For example, the global
26 burned area observed by satellite decreased 24% over the past two decades, mainly driven by
27 agricultural expansion and intensification (5). Prior to the satellite era, regional and global fire
28 trends have been reconstructed using several types of proxy records, such as charcoal from lake
29 sediments (7, 8), fire-scarred tree rings (9), and chemical impurities or trace gases preserved in ice
30 cores (10-14). However, large discrepancies remain among different records, and there is an
31 especially large uncertainty in the trend of fire emissions over the last two centuries. On the global
32 scale, the use of fossil fuel and biofuels has increased and become the major source of
33 carbonaceous aerosols, methane, ethane, and carbon monoxide in the PD, which may confound
34 interpretation of fire activity from these proxies in ice cores (10, 12, 14). Chemical transport
35 models considering these different sources are therefore needed for the interpretation of ice core
36 records. Dynamic global vegetation models have been used to simulate historical fire emissions.
37 However, different models demonstrate quite different trends of fire activity from the late
38 preindustrial Holocene to the present day, mainly because of divergent assumptions regarding the
39 response of fire to human demographic growth and to changes in land use and land cover (15-17).

40 Large uncertainty in the preindustrial aerosol loading thus results from uncertainty in
41 preindustrial fire emissions (18). Knowledge of preindustrial aerosol loading is, however, key for
42 global climate assessments that consider aerosol forcing (19). Such forcing typically quantifies the
43 present-day aerosol effect on radiative fluxes at the top of the atmosphere (TOA), relative to the
44 aerosol effect of the preindustrial (1750 or 1850 C.E.). Biomass burning emits both light-absorbing
45 (black carbon, BC) and light-scattering (organic carbon, OC) aerosols, thus directly influencing
46 the radiative balance via aerosol-radiation interactions (20). Physically and chemically aged smoke

47 particles also serve as cloud condensation nuclei (CCN), consequently altering cloud albedo and
48 indirectly affecting radiative balance via aerosol-cloud interactions (20). In addition, the cloud
49 albedo forcing of other emissions, such as fossil fuel and biofuel emissions is highly nonlinear and
50 largely depends on the CCN concentration of the preindustrial baseline, which is in turn
51 determined by preindustrial biomass burning (19).

52 In this study, we perform a comprehensive analysis of fire activity, and its associated
53 aerosol radiative forcing, for the SH over the last 250 years. We achieve this by combining an
54 array of Antarctic ice core records of BC deposition, dynamic global vegetation and fire modeling,
55 and atmospheric chemistry transport modeling. We show that BC deposition fluxes in most
56 Antarctic ice cores were roughly constant from 1750 C.E. to the present day, despite the fact that
57 other anthropogenic emissions – i.e., fossil fuel and biofuel emissions – increased dramatically in
58 the SH over the last century (21). This unexpected result can be explained by a large human-
59 induced reduction in wildfire over the same period, as suggested by the fire modeling that we
60 developed independently of the ice core records. The reduced biomass burning emissions largely
61 compensated for the increase in BC emissions from fossil fuel and biofuels.

62

63 **Results**

64 **Black carbon deposition fluxes.** We use a collection of 14 published and unpublished BC ice
65 core records retrieved throughout Antarctica (Table S1). Figure 1 shows the locations of the ice
66 core records and the BC deposition fluxes from 1750 to the present day, calculated using measured
67 BC concentrations and ice accumulation rates. A recently published Andean ice core record
68 (Illimani, Bolivia , 6300 m a.s.l., 16.7° S, 67.8° W) also is included to constrain the fire emissions
69 from the mid-to-low latitudes of South America (22) (Fig. 2). Although BC is not well mixed on

70 the hemispheric scale, different ice core records represent BC emitted from different source
71 regions across the SH and transported long distances. The simulated contribution of Antarctic BC
72 deposition from each source region is illustrated in Fig. S1. The complete array of BC ice core
73 records can thus provide constraints on the history of fire emissions at regional to hemispheric
74 scales. Compared to charcoal records that are primarily representative of local to regional fire
75 activity (7, 8), the long-range transported BC in ice cores better integrates emissions over large
76 spatial scales (14, 23). A confounding factor, however, is the increasing contribution of
77 anthropogenic fossil fuel and biofuel BC emissions during the time frame (Fig. S2) (21). In the
78 present study, these emissions are accounted for in a state-of-the-art chemical transport model
79 GEOS-Chem.

80 Measured BC deposition fluxes range from $10^0 - 10^2 \mu\text{g m}^{-2} \text{y}^{-1}$ for different ice core sites
81 across Antarctica (Table S1). The high-resolution ice core data show large year-to-year variations
82 (Fig. 1), because fire is episodic in nature, and the peaks in ice cores provide a record of the plumes
83 from large fires transported to Antarctica. However, factors other than fire emissions, such as the
84 interannual variability of atmospheric transport and precipitation may also contribute to the large
85 variability in BC flux within and across ice cores. To delineate the possible roles of climate
86 variability on the observed BC deposition fluxes, we calculate the correlation coefficients between
87 the BC flux anomalies (i.e., z-scores) and several climate indices, including the ENSO NINO3,
88 the Indian ocean dipole (IOD) mode index, and the Southern annular mode (SAM) index (Fig. S3
89 and Table S2). Although these large-scale climate variations can influence fire weather,
90 atmospheric transport, and precipitation (24, 25), most of the Antarctic ice core records do not
91 significantly correlate with these indices, indicating that the variability of BC fluxes is not driven
92 primarily by climate (Table S2). The evaluation of sea salt sodium or water isotopes records from

93 the same ice core array indicate no significant long-term changes in atmospheric transport during
94 this period, suggesting that the long-term variability of BC flux in the ice core records is driven
95 principally by the change of emissions from their source regions, likely linked to human activity.
96 For example, several ice core records indicate an increase in BC deposition flux during early 19th
97 century (Fig. 1), possibly related to land clearing during the early industrial era in the SH.
98 Moreover, most ice core records (10 out of 14) show increasing trends after 1970, consistent with
99 the rapid increase of fossil fuel and biofuel emissions quantified in historical emissions inventories
100 (21). Even so, we do not fully rule out the possibility that other processes, such as changes in
101 atmospheric circulation and precipitation, can influence the variability of individual ice core
102 records on interannual and decadal time scales. Therefore, our analysis mainly focuses on the long-
103 term historical trend of the ensemble mean of the array of Antarctic ice cores.

104 Given the complexity of BC sources, atmospheric transport, and deposition, we employ a
105 chemical transport model with detailed aerosol microphysics to aid the interpretation of the ice
106 core records (GEOS-Chem-TOMAS, see Methods). BC is short-lived in the atmosphere (~ 1 week),
107 and the model suggests that its atmospheric concentration can vary several orders of magnitudes
108 during long-range transport. To evaluate our model output, we simulate BC deposition fluxes for
109 the present-day (1998-2002) using satellite-constrained fire emissions (GFED4) (26) along with a
110 state-of-the-art fossil fuel and biofuel emissions inventory (CEDS) (21). The resulting simulated
111 BC deposition fluxes over Antarctica agree well with the contemporary BC deposition fluxes
112 derived from ice cores (1985 – 2010; Fig. S4), indicating that our model can reasonably capture
113 the magnitude and spatial heterogeneity of present-day BC deposition over Antarctica. The model
114 simulations further suggest that wet deposition involving precipitation and in-cloud scavenging is
115 the dominant BC loss pathway, contributing 87 ± 8 % (mean \pm 1 s.d.) of total BC deposition over

116 the model grid cells corresponding to the ice core sites. Dry deposition accounts for the remaining
117 modeled BC flux.

118 Despite the large temporal variabilities during the past 250 years, average BC deposition
119 fluxes derived from observations for the late preindustrial Holocene period (PI: 1750 – 1780) over
120 Antarctica are not significantly lower than those for the present-day (PD: 1985– 2010) (Figs. 1
121 and 2a). The observed PI-to-PD ratio of BC deposition flux is 0.83 ± 0.30 (mean \pm 1 s.d. for the 8
122 Antarctic ice cores with records spanning both PI and PD). This ratio is surprisingly high, given
123 the widely held view that both open biomass burning and fossil fuel/biofuel BC emissions
124 markedly increased in the SH over the last century (17, 27, 28). This discrepancy is evident in the
125 comparison between ice core observations (Fig. 2a) and the modeled BC deposition trend obtained
126 with standard CMIP6 emissions datasets – i.e., BB4CMIP (17) open biomass burning emissions
127 and CEDS (21) fossil fuel and biofuel emissions. Modeled BC deposition with CMIP6 emissions
128 shows a sharp increase from the PI to PD, with a modeled PI-to-PD ratio of 0.23 ± 0.05 (mean \pm
129 1 s.d.) over grid cells co-located with the Antarctic ice cores. This value is less than one-third of
130 the observed value. Considering that BB4CMIP uses exactly the same emissions as GFED4 for
131 the PD, and that GFED4 agrees with the ice core measurements, these results suggest that
132 simulations using the CMIP6 fire emissions underestimate PI BC deposition over Antarctica.
133 Among the Antarctic ice cores, only the record from James Ross Island at the northern tip of the
134 Antartarctic Peninsula shows a large increasing trend of BC flux (Fig. 1), with a measured PI-to-
135 PD ratio of 0.40. In contrast, the PI-to-PD ratio modeled with CMIP6 emissions for this site is just
136 0.12. The observed BC increase in James Ross Island can be explained by increasing fossil fuel
137 and biofuel emissions: sensitivity simulations suggest that more than 70% of BC deposition over

138 the island in the PD is from fossil fuel and biofuel sources, while these emissions in the PI are
139 negligible (Fig. S1).

140 We find a similar discrepancy between the model and an ice core record from the SH
141 tropics. Figure 2b shows the trend of BC flux in the Illimani ice core from the central Andes
142 (16.7°S). Model results suggest that the BC deposition in the Illimani core is primarily from open
143 biomass burning and fossil fuel/biofuel emissions in mid- to low-latitude South America, which
144 includes the Amazon rainforest. Emissions from this region are not well captured by the Antarctic
145 ice cores (Fig. S1), and thus the Illimani record complements the Antarctic records. Between 1750
146 and 1850, the Illimani record shows that the ratio of BC deposition flux relative to PD increased
147 from 0.25 to 0.6 (Fig. 2b). In comparison, the PI-to-PD ratio modeled with CMIP6 emissions is
148 about 0.08 (Fig. 2b), much lower than observed. In addition, the charcoal flux in the Illimani ice
149 core, which indicates local fire activity, exhibits a PI-to-PD ratio of 0.53 (29), in contrast to the
150 15-fold increase in BB4CMIP biomass burning emissions within a ~25 km radius of Illimani.

151 **Improved fire modeling.** Comparison between model simulations and SH ice core proxies
152 suggest that the CMIP6 inventories largely underestimate fire emissions in the preindustrial period.
153 The historical biomass burning emissions inventory for CMIP6 (BB4CMIP) (17) was constructed
154 based on different data sources. For the most recent few decades, BB4CMIP is principally driven
155 by observational datasets including GFED4 and visibility. During the preindustrial era, BB4CMIP
156 is mainly the ensemble mean of six global fire models. Importantly, most of these models assume
157 that a fire activity is positively correlated with human demographics at low to moderate population
158 densities. BB4CMIP consequently shows a slight increasing trend in fire emissions throughout the
159 SH (Figs. 3a, 3b), mainly in the low latitudes (Figs. 3c, 3d), and hemispheric total BC emission

160 increases from 0.6 TgC y⁻¹ in the PI to 1.0 TgC y⁻¹ in the PD (Fig. 3e). This trend is not consistent
161 with the ice core records.

162 To improve our understanding of historical fire emissions in the SH, here we perform a
163 new set of simulations using a process model specifically designed to represent anthropogenic fire
164 in preindustrial time. We use the LPJ-LMfire global dynamic vegetation and fire model (30) to
165 simulate fire emissions from 1750 to 2015 in a transient simulation. LPJ-LMfire represents the
166 human influence on fire through explicit simulation of managed burning carried out by agricultural
167 and pastoral societies, by accounting for changes in the size and geographic distribution of these
168 populations over time, and by representing the effects of land use on wildfire behaviour through
169 fire protection and landscape fragmentation. Even considering this passive suppression, LPJ-
170 LMfire still overestimates burned area in many regions in the PD as compared with GFED4, such
171 as Europe, Middle East, North America, and South America. To correct this systematic bias, we
172 calculated the ratio between GFED4 burned area and that simulated by LPJ-LMfire for each of the
173 17 regions (Fig. S5), and used these ratios to scale the modeled biomass burning emissions for the
174 entire period from 1750-2015 in post-processing (Methods). This region-specific correction brings
175 the simulated PD emissions into agreement with GFED4 (Fig. 3a, 3d), while keeping the historical
176 fire trend consistent with the original LPJ-LMfire transient simulation. The scaled LPJ-LMfire
177 emissions are used throughout this study.

178 Between 1750 and the early part of the 20th century, LPJ-LMfire simulates a relatively
179 stable level of fire emissions in the SH, followed by a 30% decrease until about 1990 (Fig. 3e).
180 Southern Hemisphere fire emissions are stable during the first ca. 150 years of our simulations
181 primarily because of slow demographic growth and anthropogenic land cover change; meteorology
182 adds interannual variability to the simulation but is not responsible for a secular long-term change.

183 During the 20th century, the simulated strong decline in fire emissions is caused by the rapid
184 expansion of land use for agriculture and animal production, particularly in Australia, South
185 Africa, and Argentine Patagonia (31) (Fig. 3a-b and Fig. S6). Anthropogenic landscape
186 fragmentation as a result of the conversion of natural landscapes to agriculture and rangelands is a
187 well-known form of passive fire suppression (4). Expansion of pastures and rangelands for animal
188 production has a particularly strong influence on fire, because high densities of livestock reduce
189 the amount of biomass fuels and occur in combination with landscape fragmentation from roads,
190 fence lines, paddocks, farmsteads, and other structures. In the late 20th century and up to the end
191 of our study period (2010), climate variability combined with the influence of increasing
192 atmospheric CO₂ concentrations leads to a small increase in biomass in semi-arid regions of the
193 Southern Hemisphere (e.g., 32, 33) with concomitant fire emissions.

194 After the region-specific correction, LPJ-LMfire predicts that biomass burning emissions
195 of BC over the SH decrease from 1.4 Tg y⁻¹ in the PI to 1.0 Tg y⁻¹ at PD (Fig. 3e). Most of the
196 reductions occur in higher latitudes from which emissions can be more efficiently transported to
197 Antarctica (Fig. 3c and d). During the same period, fossil fuel and biofuel BC emissions over the
198 SH increase from < 0.1 TgC y⁻¹ in the PI to 0.9 TgC y⁻¹ in the PD. Using LPJ-LMfire emissions as
199 input, the modeled PI-to-PD ratio of BC deposition is 0.97 ± 0.18 (mean ± 1 s.d.) over grid cells
200 co-located with Antarctic ice cores, in much better agreement with measurements than that
201 modeled with the CMIP6 emissions (Fig. 2a). The simulation with scaled LPJ-LMfire emissions
202 also improves the comparison with the tropical Illimani ice core. The modeled PI-to-PD ratio is
203 0.25, consistent with measurements (Fig. 2b).

204 **Implications for aerosol radiative forcing.**

205 Here we calculate the aerosol radiative forcing from all sources (i.e., biomass burning +
206 fossil fuel and biofuels) relative to 1750 at the TOA for the SH using two different biomass burning
207 emission inventories (i.e., BB4CMIP and LPJ-LMfire). We include biomass burning in the forcing
208 calculations because the change in biomass burning emissions is due largely to anthropogenic
209 activities. For both simulations, we use CEDS for anthropogenic fossil fuel and biofuel emissions.
210 The simulations are performed for 6 time slices between 1750 and 2000. Maps of direct radiative
211 forcing and cloud albedo forcing simulated for the year 2000 relative to 1750 conditions are
212 illustrated in Fig. 4. Overall, the change in total aerosol from preindustrial to the present-day has
213 a cooling effect mainly because of the increase in CEDS anthropogenic fossil fuel and biofuel
214 emissions. The differing trends in the biomass burning emission inventories, however, change the
215 sign of direct radiative forcing in some regions in the SH, such as Australia and the Amazon (Figs.
216 4a, 4b).

217 Figure 5a shows the time series of the cloud albedo forcing since 1750 owing to changes
218 in both anthropogenic and biomass burning emissions. The shaded area represents the estimated
219 uncertainty considering the error propagation from the variabilities in the input of emissions and
220 meteorology. Simulation with the LPJ-LMfire emissions yields a less negative cloud albedo
221 forcing than that with the BB4CMIP emissions. For the year 2000, the simulation with LPJ-LMfire
222 predicts a mean cloud albedo forcing of -0.33 W m^{-2} for the SH, compared with a value of -0.52
223 W m^{-2} using the BB4CMIP emissions. These results indicate that cloud albedo forcing in the SH
224 is very sensitive to the change in biomass burning emissions. The difference between BB4CMIP
225 and LPJ-LMfire biomass burning emissions also can influence estimates of the preindustrial CCN
226 number concentration in the SH (Fig. S7), thus changing the baseline of climate assessments.
227 Importantly, in the relatively clean conditions of the preindustrial SH, changes in the CCN number

228 concentration have a greater impact on cloud albedo forcing than they would under the more
229 polluted conditions of the Northern Hemisphere (Fig. S8).

230 Figure 5b depicts the values of direct radiative forcing due to aerosol-radiation interactions
231 calculated for total aerosol (i.e., including biomass burning, fossil fuel, and biofuel emissions)
232 using different biomass burning emission inventories. To separate the contributions of fossil fuel
233 and biofuel versus biomass burning aerosols, we also show the direct radiative forcing of
234 anthropogenic emissions only (Fig. 5b). The increase of anthropogenic emissions alone from 1750
235 to 2000 has a direct radiative forcing of -0.05 W m^{-2} . Over the same period, the increase in
236 biomass burning emissions suggested by BB4CMIP has an additional negative forcing of
237 -0.03 W m^{-2} , and total aerosol direct forcing is -0.08 W m^{-2} . In contrast, the total aerosol direct
238 radiative forcing calculated when using LPJ-LMfire emissions is just -0.02 W m^{-2} , indicating that
239 the positive forcing of decreasing biomass burning largely compensates the negative forcing of the
240 increasing anthropogenic emissions. These results suggest that the difference in biomass burning
241 emissions can dominate the magnitude of aerosol direct radiative forcing in the SH. Even so, the
242 values of direct radiative forcing are generally one order of magnitude smaller than those of cloud
243 albedo forcing, suggesting that the climate impact of biomass burning emissions is primarily
244 caused by the cloud albedo effect.

245

246 **Discussion**

247 The continuous high-resolution BC ice core records from Antarctica and the Andes are
248 highly complementary to previously reported Holocene records of fire proxies, such as charcoal
249 records (7, 34) as well as ice core records of carbon monoxide (CO) (10), methane (11, 12), ethane
250 (12), and levoglucosan (35). Compared with other ice core proxies, BC is chemically stable, thus

251 less susceptible to post-deposition processes. A general consensus of these other records is that the
252 global fire emissions may have been relatively high early in the past millennium (1000-1500 CE),
253 with a decreasing trend from the Medieval warm period (~1000 CE) to the Little Ice Age (LIA;
254 1600-1800 CE) (7, 10-12). However, there are large discrepancies in the reported trends of fire
255 emissions over the last two centuries. Charcoal (7) and CO (10) records suggest that global fire
256 emissions increased from the LIA minimum to a peak in late 1800s to early 1900s, followed by a
257 70% decrease in the late 20th century, although the fire modeling performed by van der Werf (2)
258 suggests that such a large reduction seems unlikely. On the contrary, the methane and ethane
259 records suggest a sharp increase in fire emissions over the last 150 years (11, 12). Our SH BC
260 records and fire modeling support our contention that the PI (1750-1850) fire emission level is 20-
261 30% higher than that of the PD (~2000). Hamilton et al. (18) also suggested greater PI fire activity
262 compared with the PD, based on several BC records from the Northern Hemisphere. These results
263 imply that extensive fire events may not be uncommon prior to 1900. Even so, our fire modeling
264 suggests that fire emissions can potentially increase in the 21st century, driven largely by the
265 warmer climate and the fertilizing effect of increasing CO₂ on vegetation, especially over
266 unmanaged land such as national forests and parks (36). A historical record of area burnt in
267 Australia shows a declining trend in the 20th century (37), followed by a significant increase since
268 2000, reaching an unprecedented level in 2019-2020 (38, 39). These fire trends are roughly
269 consistent with our model predictions.

270 These records indicate that the CMIP6 biomass burning emissions widely applied to
271 climate models may underestimate SH fire emissions in the late preindustrial era, and further affect
272 estimates of contemporary aerosol radiative forcing. With the improved biomass burning
273 emissions presented here, PI-to-PD aerosol forcing (direct radiative forcing + cloud albedo forcing)

274 in the SH changes from -0.61 W m^{-2} to -0.35 W m^{-2} , indicating that large uncertainties in aerosol
275 radiative forcing may stem from uncertainties in the historical trend in biomass burning. Similarly,
276 based on ice core records from Greenland, Europe, and North America, Hamilton et al. (18)
277 suggest that the reduction in biomass burning emissions may also occur in the Northern
278 Hemisphere.

279 As a caveat, the radiative forcing calculations we present here consider neither rapid
280 adjustments of atmosphere or surface to aerosol perturbations nor effects on cloud lifetime(20).
281 Another caveat is that the meteorological fields used as input for the fire model and chemical
282 transport model do not consider the climate feedback of the updated fire emissions. These caveats
283 could be addressed in future studies using fully-coupled Earth system models.

284 Accurate estimates of aerosol radiative forcing are also crucial for better understanding the
285 transient climate response and equilibrium climate sensitivity (i.e., TCR and ECS) to increasing
286 CO_2 , and more accurate projection of future climate change (40). The negative aerosol radiative
287 forcing can, in part, cancel out the positive forcing of increasing greenhouse gases and contribute
288 to the uncertainty of total radiative forcing. An overly large aerosol cooling implies that models
289 might overestimate TCR and ECS to reproduce historical temperature response (41). A recent
290 study using one of the latest generation CMIP6 climate models (E3SM) suggested that reducing
291 both the magnitudes of negative aerosol radiative forcing and climate sensitivity yields a better
292 agreement with the observed historical record of the surface temperature (42). Ten in twenty-seven
293 of the CMIP6 climate models have an ECS higher than the upper end of the range (1.5-4.5 °C)
294 estimated by previous generation models. These high ECS values, however, are not supported by
295 paleoclimate constraints (43). Modest aerosol forcing and climate sensitivity values have also been
296 suggested by other, observationally based studies (44, 45). Our improved fire emissions may help

297 to bridge the gap between aerosol forcing estimates from current climate model simulations and
298 the constraints from observations.

Materials and Methods

Ice core measurements. Details of ice cores included in the Desert Research Institute (DRI) Antarctic array are listed in Table S1. All ice cores were analyzed using the well-established DRI method for continuous BC measurements(14, 46, 47). In brief, BC concentrations were measured in a continuous stream of ice-core meltwater by coupling a nebulizer to a Single Particle Soot Photometer (SP2; Droplet Measurement Technologies, Boulder, CO, USA). Annual depositional fluxes were determined using net water-equivalent snowfall rates derived from annual layer thickness(48) and measured density profiles following standard procedures. Note that modern ice-core derived accumulation rates over Antarctica (Fig. S9) agree well with precipitation rates from the reanalysis dataset (MERRA2) used for model simulations. All of the ice core records were mapped from depth to year using either volcanically constrained annual layer counting or volcanic synchronization followed by linear interpolation(23), with non-sea-salt-sulfur in the WAIS Divide record on the WD2014 age scale(49) serving as the reference.

LPJ-LMfire. The LPJ-LMfire dynamic global vegetation model (30) includes processes to simulate natural wildfires from lightning ignition and a unique representation of anthropogenic fire caused by preindustrial societies, which distinguishes the different relationships between humans and fire among hunter-gatherers, pastoralists, and farmers. To run the model, we developed a transient climate scenario by combining climatological mean climate fields that provide a high-spatial-resolution baseline with monthly climate anomalies from simulations of the GISS Model E2R earth system model. The GISS meteorology used to drive LPJ-LMfire combined ensemble results from simulations of the past millennium (850-1850)(50), historical period (1850-2005)(51), and RCP4.5 (2006-2100)(52) prepared for CMIP5. We generated monthly anomalies for the period 1701-2015 relative to a 1961-1990 averaging period. These anomalies were added to the high-resolution climate fields described in Table 3 of Pfeiffer et al. (30). Further details of the protocol we used to prepare the input climate datasets were described in Hamilton et al. (18).

To capture the effects of land use, we merged the KK10 anthropogenic land cover change scenario (53), which ends in 1850, with the HYDE 3.2 dataset (54), following the protocol described in Kaplan et al. (55). LPJ-LMfire included a representation of managed fire on agricultural and rangelands in which 50% of the litter on 20% of managed land (cropland and rangeland) was burned annually. Wildfire did not otherwise occur on managed land in the model, and wildfire ignitions were caused only by lightning or foraging people (for further details see 30).

To perform a PD simulation with LMfire, we made a transient model simulation for the period 1701-2015 driven by the climate and land use time series described above and reconstructed atmospheric CO₂ concentrations. We performed the LPJ-LMfire simulation continuously over our study period and archived model state variables with monthly resolution. The spatial resolution of the model output was 0.5°×0.5°. The land cover change used in LPJ-LMfire model is shown in Fig. S6. There was a large increase in pasture in the temperate Southern Hemisphere (~30 °S) starting in 1880s and intensifying through the 20th century. The crop land area also increased significantly in the 20th century. Modern agricultural technology and air quality legislation can largely suppress fire on human-used land. Therefore, cropland or pasture do not burn or burn much less than natural vegetation. This land cover change, along with associated landscape

fragmentation caused a reduction in fire activity for an increase of human-managed land. For example, the rapid expansion of land use for agriculture and animal production in the Southern Hemisphere resulted in a strong decline in fire emissions over Australia, South Africa, and Argentine Patagonia in the late 20th century (Fig. 4).

To further reduce systematic biases in the fire model output, we scaled the output for each region to the GFED4 burned area for the overlapping 1997-2015 period. This scaling method was similar to that used in BB4CMIP for the FireMIP model output (17). However, we used burned areas instead of carbon emissions for the scaling, as GFED4 burned areas were from satellite observations and so more accurate. We divided the globe into 17 fire regions, consistent with the definitions in BB4CMIP. To derive fire emissions, we combined the regional scaled dry matter burned for different vegetation types from LMfire with the emission factors from Akagi et al. (56) and Andreae and Merlet. (57) These emission factors are consistent with those used in BB4CMIP (17) and GFED4 (26).

GEOS-Chem-TOMAS simulations. We implemented the historical fire (i.e., BB4CMIP (17), LPJ-LMfire) and anthropogenic (CEDS (21)) emissions into the 3D, global chemical transport model GEOS-Chem, version 12 (http://wiki.seas.harvard.edu/geos-chem/index.php/GEOS-Chem_12). The version of GEOS-Chem used in this study had 47 vertical layers and $4^\circ \times 5^\circ$ horizontal resolution and was driven by meteorology from the Modern-Era Retrospective analysis for Research and Applications, version 2 (MERRA-2) from the NASA Global Modeling and Assimilation Office (GMAO). To simulate aerosol number, mass, and size distributions in the atmosphere, we coupled GEOS-Chem with the Two Moment Aerosol Sectional (TOMAS) (58) microphysics module. The TOMAS module used 15 size bins ranging from 3 nm to 10 μm for aerosol components of sulfate, organic aerosols, BC, sea salt, and dust (59). TOMAS simulated particle nucleation, coagulation, growth, and wet and dry deposition. In addition to biomass burning and anthropogenic emissions, GEOS-Chem included emissions for biogenic secondary organic aerosols (SOA; MEGAN 2.1 (60) with a simple scheme for SOA formation (61)), sea salt (62), volcanic aerosol (Aerocom), and wind-blown dust (DEAD) (63). GEOS-Chem-TOMAS was validated against global measurements of aerosol number concentration and size distribution (64).

We performed simulations for six time slices between 1750 and 2000 at 50-year intervals. For each time slice, the simulation was carried out for 5.5 years using 1998-2002 meteorology but changing emissions. Applying present-day meteorology allowed us to isolate the effect of changing emissions. Results from the first 6-months in each time slice were discarded, and the remaining results used for analysis. The output of size-resolved aerosol compositions in the atmosphere and deposition fluxes were archived monthly. Modeled results were shown as 5-yr averages, and year-to-year variations were used to estimate the uncertainty in natural variabilities in meteorology and emissions. Using the monthly output of GEOS-Chem-TOMAS, we derived the hygroscopicity parameter κ as a volume-weighted mean of each individual species. We used the κ value for each size bin and particle number size distribution to calculate the CCN number concentration at a supersaturation of 0.2%.

Aerosol radiative forcing. The all-sky direct radiative effect and cloud albedo effect were calculated at the top of the atmosphere (TOA) based on the monthly size-resolved aerosol output from GEOS-Chem-TOMAS. Details of these calculations are in Kodros et al. (65) To derive the direct radiative effect, we first calculated aerosol optical properties, including aerosol optical depth (AOD), single-scattering albedo (SSA), and asymmetry factor using Mie code (66). We assumed an external mixture of BC with other species in the Mie calculations. To take into account the

possible lensing effect of core-shell mixing, we multiplied the calculated absorption coefficient by a constant absorption enhancement factor of 1.5 (67). The calculated optical properties were then used as input to the offline version of the Rapid Radiative Transfer Model for Global climate models (RRTMG). Using the TOA shortwave and longwave fluxes, we calculated the aerosol direct radiative effect as referenced to an aerosol-free condition.

For the cloud albedo effect, we used the sectional representation of cloud activation from Abdul-Razzak and Ghan (68) to calculate cloud droplet number concentrations (CDNCs) for a updraft velocity of 0.3 m s^{-1} . The cloud activation scheme took monthly data of particle number size distribution and size-resolved κ values as input. As a control, a uniform cloud droplet radius of $10 \text{ }\mu\text{m}$ was assumed for the PD, consistent with the satellite measurements of ISCCP. The effective radii of low and mid-level clouds (up to 600 hPh) were perturbed by taking the ratio of CDNC between historical and PD to the one-third power. The implied assumption is that aerosol did not change the liquid water path, as the definition of the cloud-albedo aerosol indirect effect (i.e., first indirect effect or Twomey effect). The change in radiative fluxes at TOA due to the change in cloud effective radius was calculated by offline RRTMG. We did not consider the aerosol effect on cloud lifetime. Both direct radiative forcing and cloud albedo forcing were defined as the differences in the present-day aerosol effect relative to the preindustrial baseline (1750), considering changes in all aerosols including biomass burning, fossil fuel, and biofuel emissions.

Acknowledgments. This research primarily was funded by the Geosciences Directorate of the National Science Foundation under grants AGS-1702814 and 1702830, with additional support from 0538416, 0538427, and 0839093. We thank students and staff of the DRI ice-core laboratory, as well as U.S. and other field teams. B53 and B40 ice-core samples were provided by the Alfred-Wegener-Institut, James Ross Island and Gomez samples by the British Antarctic Survey, and Aurora Basin and W10 samples by the Australian Antarctic Division.

Author contributions. P.L., L.J.M., J.O.K., and J.R.M. designed the study. N.J.C., M.M.A., M.S., and J.R.M. carried out black carbon measurements using Antarctic ice core samples provided by J.F., R.M., and M.A.J.C. M.S. provided Illimani ice core dataset. J.O.K., P.L., and Y.L. performed LPJ-LMfire simulations and prepared fire emissions data. P.L. performed GEOS-Chem-TOMAS simulations. P.L., J.K.K., and J.R.P. performed radiative forcing calculations. P.L., J.O.K., L.J.M., and J.R.M. led the manuscript writing with specific comments and edits from all other co-authors.

The authors declare no conflict of interests.

Data availability. The datasets generated during and/or analysed during the current study are available from the corresponding author on reasonable request.

Code availability. The Python codes used in this paper to analyze ice core data, prepare emissions inventory, perform radiative forcing calculations, and produce the figures are available from the corresponding author on reasonable request.

Correspondence to Pengfei Liu (Pengfei.liu@eas.gatech.edu)

List of Figures

Figure 1. Preindustrial-to-present variations of the black carbon deposition mass fluxes derived from an Antarctic-wide array of synchronized high-resolution ice core records. Gray curves represent annual mean black carbon fluxes from different ice cores. Thick black curves represent the 30-year running average values. Different symbols represent the ice core locations. Age uncertainty is estimated to be less than ± 1 year to ± 3 years.

Figure 2. Measured and modeled trends of black carbon deposition fluxes over Antarctica (a) and Bolivia Andes (b). The trends are shown as the ratios of historical black carbon fluxes to present-day values (centered around the year 2000). Thick curves in (a) represent the median values of 12 ice core records or co-located modeled results. Shaded areas in (a) represent the 25th to 75th percentile range across sites. The black curve in (b) represents the 30-year running average of black carbon ratios in an Andean ice core record from Illimani, Bolivia(22). The gray curve represents annually averaged values. Modeled values in both panels are from GEOS-Chem-TOMAS simulations using two different biomass burning emission inventories – Biomass burning for CMIP6 (blue)(17) and LPJ-LMfire (orange). Fossil fuel and biofuel emissions are from the Community Emissions Data System (CEDS) for CMIP6(21). Shaded areas in (b) represent the standard deviation across different years.

Figure 3. Preindustrial to present-day changes of black carbon emissions from biomass burning in the Southern Hemisphere. (a) Maps show the annually averaged black carbon emission fluxes from biomass burning for preindustrial (1750-1780) and

present-day (1998-2014). (b) Maps show the preindustrial to present-day changes of black carbon emission fluxes. Zonal mean black carbon emissions are shown for preindustrial period in (c), and for the present day in (d). (e) Annual mean black carbon emissions from biomass burning in the Southern Hemisphere from 1750 to 2014. Biomass burning emissions are from the historical biomass burning emissions for CMIP6 (blue, BB4CMIP) (17) and a fire model coupled with a dynamic global vegetation model (orange, LPJ-LMfire) (30). The PD emissions from BB4CMIP are the same as the GFED4 data set. Fossil fuel and biofuel emissions of black carbon from CEDS are shown in red in panels (c)-(e) for comparison. Maps in (a) and (b) are displayed for the Southern Hemisphere using south pole stereographic projection to emphasize the spatial variation in emissions across biomass burning regions.

Figure 4. Aerosol direct radiative forcing calculated by the RRTMG radiative transfer model using GEOS-Chem-TOMAS model output simulated with (a) CEDS fossil fuel and biofuel emissions and BB4CMIP biomass burning emissions, and (b) CEDS and LPJ-LMfire biomass burning emissions. Cloud albedo forcing simulated with (c) CEDS and BB4CMIP emissions, and (d) CEDS and LPJ-LMfire emissions. Radiative forcing values are calculated for the year 2000 relative to 1750 conditions.

Figure 5. Southern hemisphere annual mean aerosol cloud albedo forcing (a) and direct radiative forcing (b) since the pre-industrial era (1750). The forcing calculations incorporate changes in biomass burning, fossil fuel, and biofuel emissions. Open markers represent the model calculated values using GEOS-Chem-TOMAS and RRTMG (see Methods). Solid curves represent interpolated values based on the

anthropogenic SO₂ emissions from CEDS (red) and the biomass burning OC emissions from LPJ-LMfire (orange) and BB4CMIP (blue). Shading areas represent the uncertainty considering the variability of emissions.

References

1. O. Pechony, D. T. Shindell, Driving forces of global wildfires over the past millennium and the forthcoming century. *Proceedings of the National Academy of Sciences* **107**, 19167-19170 (2010).
2. G. R. van der Werf, W. Peters, T. T. van Leeuwen, L. Giglio, What could have caused pre-industrial biomass burning emissions to exceed current rates? *Clim. Past* **9**, 289-306 (2013).
3. L. E. O. C. Aragão *et al.*, Interactions between rainfall, deforestation and fires during recent years in the Brazilian Amazonia. *Philosophical transactions of the Royal Society of London. Series B, Biological sciences* **363**, 1779-1785 (2008).
4. S. Archibald, D. P. Roy, B. W. Van Wilgen, R. J. Scholes, What limits fire? An examination of drivers of burnt area in Southern Africa. *Global Change Biology* **15**, 613-630 (2009).
5. N. Andela *et al.*, A human-driven decline in global burned area. *Science* **356**, 1356-1362 (2017).
6. I. Bistinas, S. P. Harrison, I. C. Prentice, J. M. C. Pereira, Causal relationships versus emergent patterns in the global controls of fire frequency. *Biogeosciences* **11**, 5087-5101 (2014).
7. J. R. Marlon *et al.*, Climate and human influences on global biomass burning over the past two millennia. *Nature Geoscience* **1**, 697-702 (2008).
8. J. R. Marlon *et al.*, Reconstructions of biomass burning from sediment-charcoal records to improve data–model comparisons. *Biogeosciences* **13**, 3225-3244 (2016).
9. A. Holz, S. Haberle, T. T. Veblen, R. De Pol-Holz, J. Southon, Fire history in western Patagonia from paired tree-ring fire-scar and charcoal records. *Clim. Past* **8**, 451-466 (2012).
10. Z. Wang, J. Chappellaz, K. Park, J. E. Mak, Large Variations in Southern Hemisphere Biomass Burning During the Last 650 Years. *Science* **330**, 1663-1666 (2010).
11. D. F. Ferretti *et al.*, Unexpected Changes to the Global Methane Budget over the Past 2000 Years. *Science* **309**, 1714-1717 (2005).
12. M. R. Nicewonger, M. Aydin, M. J. Prather, E. S. Saltzman, Large changes in biomass burning over the last millennium inferred from paleoatmospheric ethane in polar ice cores. *Proceedings of the National Academy of Sciences* **115**, 12413-12418 (2018).
13. M. Legrand *et al.*, Boreal fire records in Northern Hemisphere ice cores: a review. *Clim. Past* **12**, 2033-2059 (2016).
14. J. R. McConnell *et al.*, 20th-Century Industrial Black Carbon Emissions Altered Arctic Climate Forcing. *Science* **317**, 1381-1384 (2007).
15. F. Li *et al.*, Historical (1700–2012) global multi-model estimates of the fire emissions from the Fire Modeling Intercomparison Project (FireMIP). *Atmos. Chem. Phys.* **19**, 12545-12567 (2019).
16. S. Hantson *et al.*, The status and challenge of global fire modelling. *Biogeosciences* **13**, 3359-3375 (2016).
17. M. J. E. van Marle *et al.*, Historic global biomass burning emissions for CMIP6 (BB4CMIP) based on merging satellite observations with proxies and fire models (1750–2015). *Geosci. Model Dev.* **10**, 3329-3357 (2017).
18. D. S. Hamilton *et al.*, Reassessment of pre-industrial fire emissions strongly affects anthropogenic aerosol forcing. *Nature Communications* **9**, 3182 (2018).

19. K. S. Carslaw *et al.*, Large contribution of natural aerosols to uncertainty in indirect forcing. *Nature* **503**, 67-71 (2013).
20. T. Stocker, *Climate change 2013: the physical science basis: Working Group I contribution to the Fifth assessment report of the Intergovernmental Panel on Climate Change*. (Cambridge University Press, 2014).
21. R. M. Hoesly *et al.*, Historical (1750–2014) anthropogenic emissions of reactive gases and aerosols from the Community Emissions Data System (CEDS). *Geosci. Model Dev.* **11**, 369-408 (2018).
22. D. Osmont, M. Sigl, A. Eichler, T. M. Jenk, M. Schwikowski, A Holocene black carbon ice-core record of biomass burning in the Amazon Basin from Illimani, Bolivia. *Clim. Past* **15**, 579-592 (2019).
23. J. R. McConnell *et al.*, Antarctic-wide array of high-resolution ice core records reveals pervasive lead pollution began in 1889 and persists today. *Scientific Reports* **4**, 5848 (2014).
24. H. Purdie *et al.*, Interannual variability in net accumulation on Tasman Glacier and its relationship with climate. *Global and Planetary Change* **77**, 142-152 (2011).
25. W. Cai, T. Cowan, M. Raupach, Positive Indian Ocean Dipole events precondition southeast Australia bushfires. *Geophysical Research Letters* **36**, (2009).
26. G. R. van der Werf *et al.*, Global fire emissions estimates during 1997–2016. *Earth Syst. Sci. Data* **9**, 697-720 (2017).
27. J. F. Lamarque *et al.*, Historical (1850–2000) gridded anthropogenic and biomass burning emissions of reactive gases and aerosols: methodology and application. *Atmos. Chem. Phys.* **10**, 7017-7039 (2010).
28. F. Dentener *et al.*, Emissions of primary aerosol and precursor gases in the years 2000 and 1750 prescribed data-sets for AeroCom. *Atmos. Chem. Phys.* **6**, 4321-4344 (2006).
29. S. O. Brugger *et al.*, Tropical Andean glacier reveals colonial legacy in modern mountain ecosystems. *Quaternary Science Reviews* **220**, 1-13 (2019).
30. M. Pfeiffer, A. Spessa, J. O. Kaplan, A model for global biomass burning in preindustrial time: LPJ-LMfire (v1.0). *Geosci. Model Dev.* **6**, 643-685 (2013).
31. N. Ramankutty, J. A. Foley, Estimating historical changes in global land cover: Croplands from 1700 to 1992. *Global Biogeochemical Cycles* **13**, 997-1027 (1999).
32. B. Poulter *et al.*, Contribution of semi-arid ecosystems to interannual variability of the global carbon cycle. *Nature* **509**, 600-603 (2014).
33. A. L. Skowno *et al.*, Woodland expansion in South African grassy biomes based on satellite observations (1990-2013): general patterns and potential drivers. *Glob Chang Biol* **23**, 2358-2369 (2017).
34. J. R. Marlon *et al.*, Global biomass burning: a synthesis and review of Holocene paleofire records and their controls. *Quaternary Science Reviews* **65**, 5-25 (2013).
35. D. Battistel *et al.*, High-latitude Southern Hemisphere fire history during the mid- to late Holocene (6000–750 BP). *Clim. Past* **14**, 871-886 (2018).
36. Y. Li, L. J. Mickley, P. Liu, J. O. Kaplan, Trends and spatial shifts in lightning fires and smoke concentrations in response to 21st century climate over the national forests and parks of the western United States. *Atmos. Chem. Phys.* **20**, 8827-8838 (2020).
37. S. Roxburgh, N. Surawski, J. Raison, H. Luck, Native forest wildfire emissions background level and margin–review of methodological options and implications for emissions reporting. *Report prepared for the Department of the Environment*, (2014).

38. M. M. Boer, V. Resco de Dios, R. A. Bradstock, Unprecedented burn area of Australian mega forest fires. *Nature Climate Change* **10**, 171-172 (2020).
39. D. B. Lindenmayer, C. Taylor, New spatial analyses of Australian wildfires highlight the need for new fire, resource, and conservation policies. *Proceedings of the National Academy of Sciences* **117**, 12481-12485 (2020).
40. P. M. Forster *et al.*, Evaluating adjusted forcing and model spread for historical and future scenarios in the CMIP5 generation of climate models. *Journal of Geophysical Research: Atmospheres* **118**, 1139-1150 (2013).
41. G. A. Meehl *et al.*, Context for interpreting equilibrium climate sensitivity and transient climate response from the CMIP6 Earth system models. *Science Advances* **6**, eaba1981 (2020).
42. J.-C. Golaz *et al.*, The DOE E3SM Coupled Model Version 1: Overview and Evaluation at Standard Resolution. *Journal of Advances in Modeling Earth Systems* **11**, 2089-2129 (2019).
43. J. Zhu, C. J. Poulsen, B. L. Otto-Bliesner, High climate sensitivity in CMIP6 model not supported by paleoclimate. *Nature Climate Change* **10**, 378-379 (2020).
44. B. Stevens, Rethinking the Lower Bound on Aerosol Radiative Forcing. *Journal of Climate* **28**, 4794-4819 (2015).
45. P. M. Cox, C. Huntingford, M. S. Williamson, Emergent constraint on equilibrium climate sensitivity from global temperature variability. *Nature* **553**, 319-322 (2018).
46. M. M. Bisiaux *et al.*, Variability of black carbon deposition to the East Antarctic Plateau, 1800–2000 AD. *Atmos. Chem. Phys.* **12**, 3799-3808 (2012).
47. M. M. Arienzo *et al.*, Holocene black carbon in Antarctica paralleled Southern Hemisphere climate. *Journal of Geophysical Research: Atmospheres* **122**, 6713-6728 (2017).
48. M. Sigl *et al.*, The WAIS Divide deep ice core WD2014 chronology – Part 2: Annual-layer counting (0–31 ka BP). *Clim. Past* **12**, 769-786 (2016).
49. M. Sigl *et al.*, Timing and climate forcing of volcanic eruptions for the past 2,500 years. *Nature* **523**, 543-549 (2015).
50. G. A. Schmidt *et al.*, Climate forcing reconstructions for use in PMIP simulations of the last millennium (v1.0). *Geosci. Model Dev.* **4**, 33-45 (2011).
51. G. A. Schmidt *et al.*, Configuration and assessment of the GISS ModelE2 contributions to the CMIP5 archive. *Journal of Advances in Modeling Earth Systems* **6**, 141-184 (2014).
52. L. Nazarenko *et al.*, Future climate change under RCP emission scenarios with GISS ModelE2. *Journal of Advances in Modeling Earth Systems* **7**, 244-267 (2015).
53. J. O. Kaplan *et al.*, Holocene carbon emissions as a result of anthropogenic land cover change. *The Holocene* **21**, 775-791 (2010).
54. K. Klein Goldewijk, A. Beusen, J. Doelman, E. Stehfest, Anthropogenic land use estimates for the Holocene – HYDE 3.2. *Earth Syst. Sci. Data* **9**, 927-953 (2017).
55. J. O. Kaplan, K. M. Krumhardt, N. E. Zimmermann, The effects of land use and climate change on the carbon cycle of Europe over the past 500 years. *Global Change Biology* **18**, 902-914 (2012).
56. S. K. Akagi *et al.*, Emission factors for open and domestic biomass burning for use in atmospheric models. *Atmos. Chem. Phys.* **11**, 4039-4072 (2011).

57. M. O. Andreae, P. Merlet, Emission of trace gases and aerosols from biomass burning. *Global Biogeochemical Cycles* **15**, 955-966 (2001).
58. P. J. Adams, J. H. Seinfeld, Predicting global aerosol size distributions in general circulation models. *Journal of Geophysical Research: Atmospheres* **107**, AAC 4-1-AAC 4-23 (2002).
59. Y. H. Lee, J. R. Pierce, P. J. Adams, Representation of nucleation mode microphysics in a global aerosol model with sectional microphysics. *Geosci. Model Dev.* **6**, 1221-1232 (2013).
60. A. B. Guenther *et al.*, The Model of Emissions of Gases and Aerosols from Nature version 2.1 (MEGAN2.1): an extended and updated framework for modeling biogenic emissions. *Geosci. Model Dev.* **5**, 1471-1492 (2012).
61. P. S. Kim *et al.*, Sources, seasonality, and trends of southeast US aerosol: an integrated analysis of surface, aircraft, and satellite observations with the GEOS-Chem chemical transport model. *Atmos. Chem. Phys.* **15**, 10411-10433 (2015).
62. L. Jaeglé, P. K. Quinn, T. S. Bates, B. Alexander, J. T. Lin, Global distribution of sea salt aerosols: new constraints from in situ and remote sensing observations. *Atmos. Chem. Phys.* **11**, 3137-3157 (2011).
63. T. Duncan Fairlie, D. J. Jacob, R. J. Park, The impact of transpacific transport of mineral dust in the United States. *Atmospheric Environment* **41**, 1251-1266 (2007).
64. J. K. Kodros, J. R. Pierce, Important global and regional differences in aerosol cloud-albedo effect estimates between simulations with and without prognostic aerosol microphysics. *Journal of Geophysical Research: Atmospheres* **122**, 4003-4018 (2017).
65. J. K. Kodros, R. Cucinotta, D. A. Ridley, C. Wiedinmyer, J. R. Pierce, The aerosol radiative effects of uncontrolled combustion of domestic waste. *Atmos. Chem. Phys.* **16**, 6771-6784 (2016).
66. C. F. Bohren, D. R. Huffman, *Absorption and scattering of light by small particles*. (John Wiley & Sons, 2008).
67. X. Wang *et al.*, Exploiting simultaneous observational constraints on mass and absorption to estimate the global direct radiative forcing of black carbon and brown carbon. *Atmos. Chem. Phys.* **14**, 10989-11010 (2014).
68. H. Abdul-Razzak, S. J. Ghan, A parameterization of aerosol activation 3. Sectional representation. *Journal of Geophysical Research: Atmospheres* **107**, AAC 1-1-AAC 1-6 (2002).
69. M. Sigl *et al.*, Insights from Antarctica on volcanic forcing during the Common Era. *Nature Climate Change* **4**, 693-697 (2014).
70. M. M. Bisiaux *et al.*, Changes in black carbon deposition to Antarctica from two high-resolution ice core records, 1850–2000 AD. *Atmos. Chem. Phys.* **12**, 4107-4115 (2012).

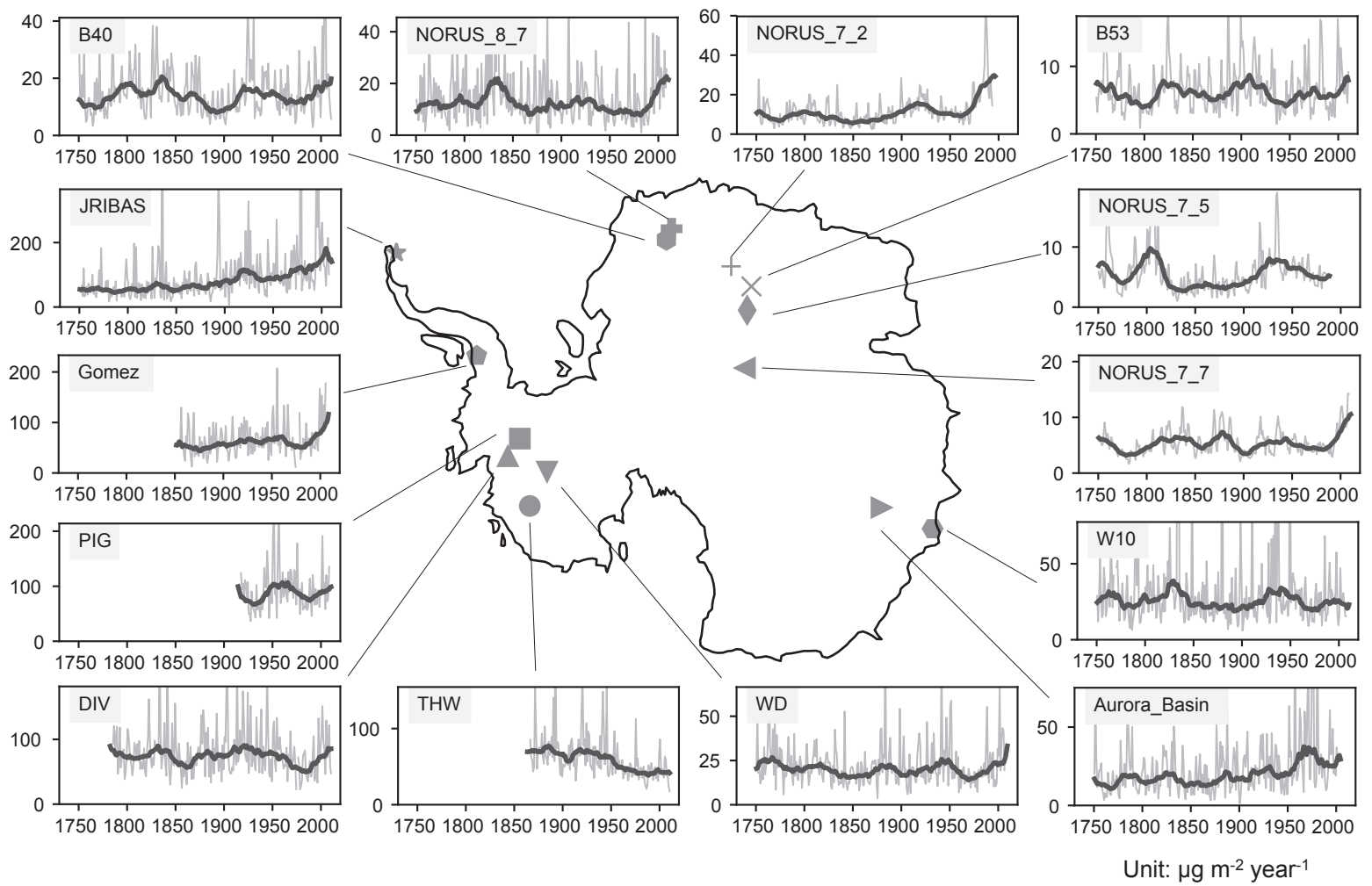


Figure 1

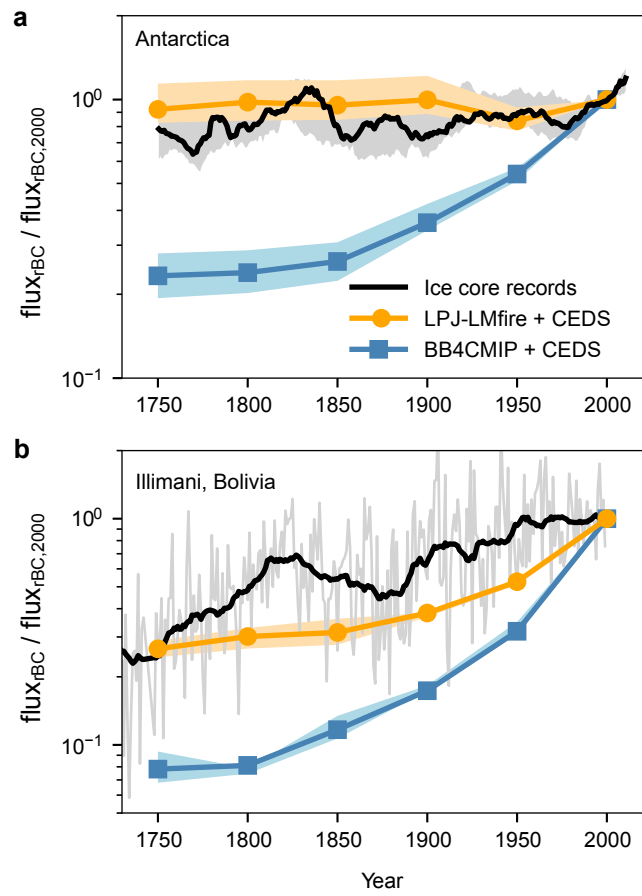


Figure 2

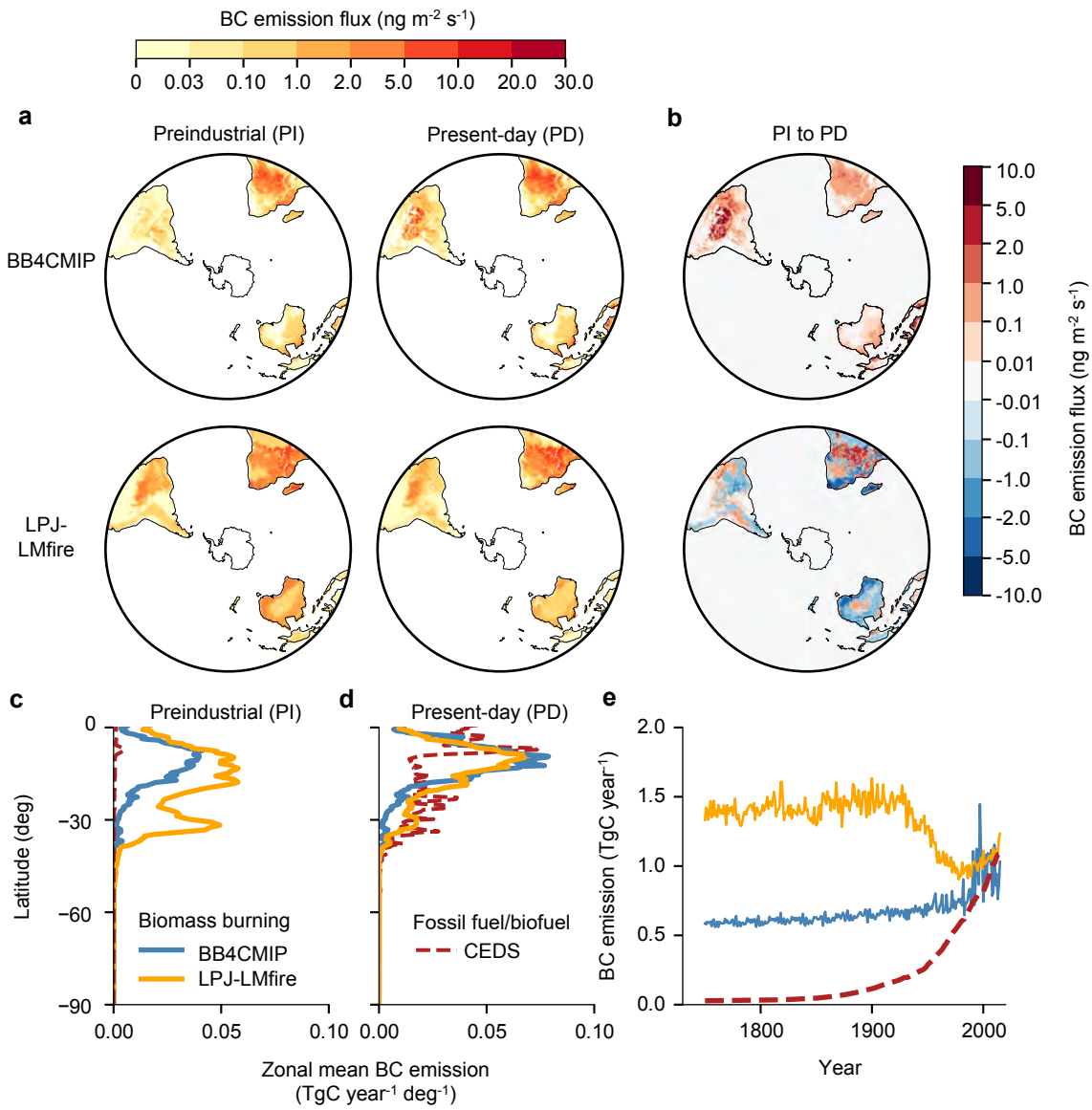
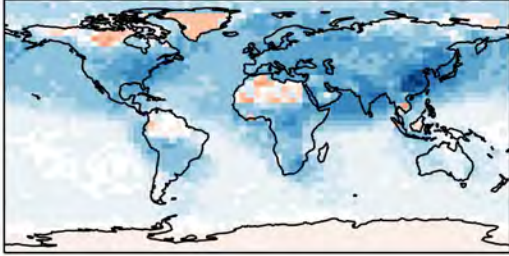
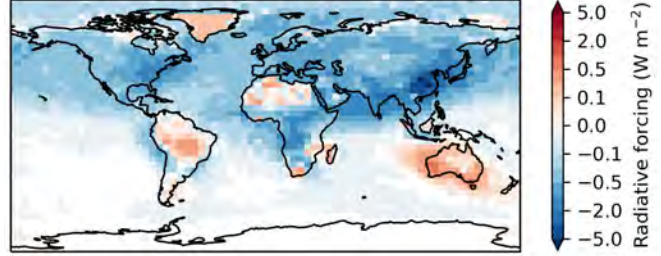


Figure 3

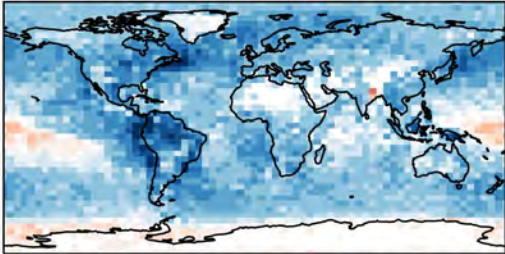
a. Direct radiative forcing, BB4CMIP + CEDS



b. Direct radiative forcing, LPJ-LMfire + CEDS



c. Cloud albedo forcing, BB4CMIP + CEDS



d. Cloud albedo forcing, LPJ-LMfire + CEDS

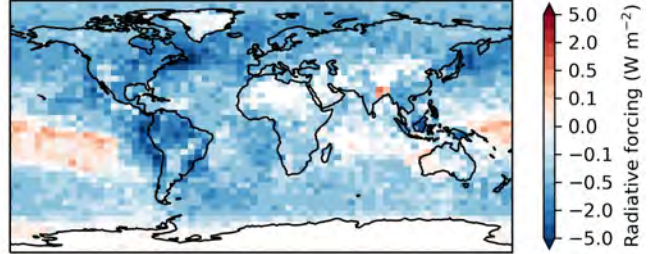


Figure 4

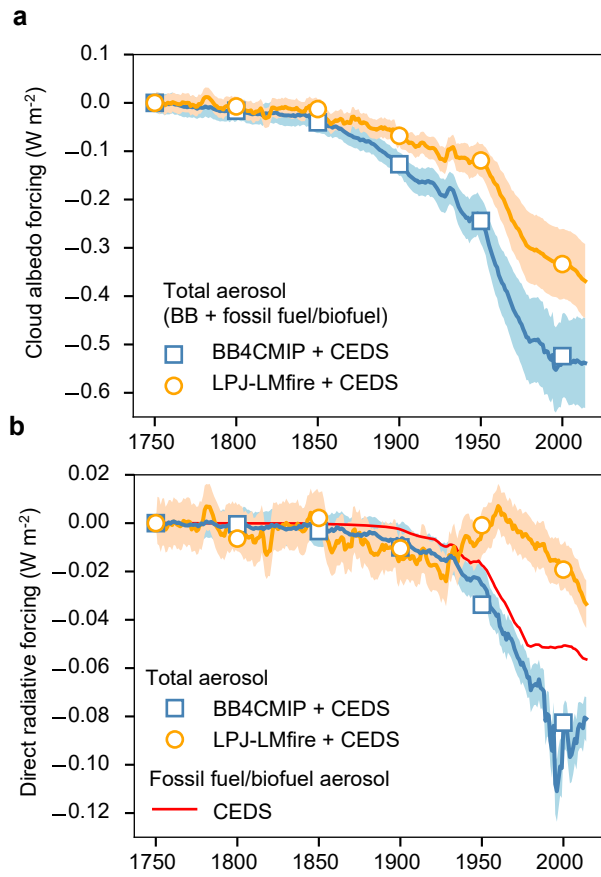


Figure 5

Supporting Information for

**Improved Estimates of Preindustrial Biomass Burning Reduce the Magnitude
of Aerosol Climate Forcing in the Southern Hemisphere**

Pengfei Liu (1,2)*, Jed O. Kaplan (3), Loretta J. Mickley (1), Yang Li (1), Nathan J. Chellman (4),
Monica M. Arienzo (4), John K. Kodros (5), Jeffrey R. Pierce (5), Michael Sigl (6,7), Johannes Freitag
(8), Robert Mulvaney (9), Mark A. J. Curran (10), and Joseph R. McConnell (4,11)

- (1) School of Engineering and Applied Sciences, Harvard University, Cambridge, MA, 02138, USA
- (2) School of Earth and Atmospheric Sciences, Georgia Institute of Technology, Atlanta, GA, 30332, USA
- (3) Department of Earth Sciences, The University of Hong Kong, Hong Kong, China
- (4) Division of Hydrologic Sciences, Desert Research Institute, NV 89512, USA
- (5) Department of Atmospheric Science, Colorado State University, Fort Collins, Colorado 80523, USA
- (6) Oeschger Centre for Climate Change Research, University of Bern, 3012 Bern, Switzerland
- (7) Climate and Environmental Physics, University of Bern, 3012 Bern, Switzerland
- (8) Alfred-Wegener-Institut Helmholtz-Zentrum für Polar- und Meeresforschung, Bremerhaven, Germany
- (9) British Antarctic Survey, Cambridge, UK
- (10) Australian Antarctic Division and Antarctic Climate and Ecosystem Cooperative Research Centre, Hobart, Tasmania, Australia
- (11) Sir Nicholas Shackleton Visiting Fellow, Clare Hall, University of Cambridge, CB3 9AL Cambridge, United Kingdom

Contains: 2 table and 9 figures

Table S1. Location, accumulation rate, and black carbon (BC) mass fluxes for different ice cores in Antarctica used in this study. BC fluxes are shown as mean \pm s.d for 30-year data.

Site	Latitude (deg N)	Longitude (deg E)	Accumulation rate (kg m ⁻² y ⁻¹)	PI BC flux (1750-1780; μ g m ⁻² y ⁻¹)	PD BC flux (1985-2015; μ g m ⁻² y ⁻¹)	References	
						BC measurement	Chronology
B53	-76.8	31.9	29	7.0 \pm 3.8	6.6 \pm 3.6	This study	This study
B40	-75.0	0.1	68	12.5 \pm 7.8	20.1 \pm 14.9	Arienzo et al. (2017)(47)	Sigl et al. (2015)(49)
NORUS_7_5	-78.6	35.6	24	6.0 \pm 4.1	n/a	Bisiaux et al. (2012a)(46)	Sigl et al. (2014)(69)
NORUS_7_7	-82.1	54.9	30	5.0 \pm 1.6	7.4 \pm 3.4	Bisiaux et al. (2012a)(46)	Sigl et al. (2014)(69)
NORUS_7_2	-76.1	22.5	33	9.3 \pm 5.5	33.5 \pm 17.3	Bisiaux et al. (2012a)(46)	Sigl et al. (2014)(69)
NORUS_8_7	-74.1	1.6	86	14.4 \pm 8.6	19.7 \pm 12.0	This study	Sigl et al. (2014)(69)
Aurora Basin	-71.2	111.4	112	17.0 \pm 13.7	27.6 \pm 13.1	This study	McConnell et al (2014)(23)
James Ross Island	-64.2	-57.7	530	63.3 \pm 31.7	161.9 \pm 114.4	This study	This study
WAIS Divide	-79.5	-112.1	210	26.8 \pm 15.1	26.9 \pm 14.8	Bisiaux et al. (2012b)(70)	Sigl et al. (2015)(49)
DIV	-76.8	-101.7	372	n/a	73.6 \pm 34.2	This study	McConnell et al (2014)(23)
THW	-77.0	-121.2	272	n/a	42.8 \pm 15.6	This study	McConnell et al (2014)(23)
PIG	-78.0	-96.0	398	n/a	89.2 \pm 31.6	This study	McConnell et al (2014)(23)
Gomez	-73.6	-70.4	690	n/a	84.5 \pm 40.8	This study	McConnell et al (2014)(23)
W10	-66.8	111.6	352	30.4 \pm 14.2	28.3 \pm 15.0	This study	Sigl et al. (2014)(69)

Table S2. Correlation coefficients between the z-scores of black carbon ice core records and climate indices. Statistically significant correlations are marked in bold (* $p < 0.05$; ** $p < 0.01$).

Site	ENSO NINO3	South Annular Model (SAM)	Indian Ocean Dipole (IOD)
B53	0.12	0.19	-0.04
B40	0.03	0.13	0.14
NORUS_7_5	-0.10	0.08	0.02
NORUS_7_7	-0.10	0.35*	0.25**
NORUS_7_2	0.13	0.09	0.21*
NORUS_8_7	0.07	0.18	0.14
Aurora Basin	-0.04	-0.32*	0.11
James Ross Island	-0.13	0.08	0.07
WAIS Divide	-0.01	0.05	0.02
DIV	0.04	-0.06	-0.02
THW	-0.04	-0.14	-0.25**
PIG	-0.11	-0.17	-0.00
Gomez	-0.12	0.32*	0.10
W10	-0.13	0.08	-0.07
Mean of 14 records	-0.08	0.09	0.14

List of Supplementary Figures

Figure S1. Modeled contributions of Antarctic BC deposition from anthropogenic fossil fuel/biofuel emissions and open biomass burning emissions from different regions in the Southern Hemisphere. The simulations are performed using GEOS-Chem-TOMAS with CEDS anthropogenic fossil fuel and biofuel emissions and LPJ-LMfire biomass burning emissions (see Methods). Gray dots represent the locations of ice core sites. The biomass burning regions in the Southern Hemisphere are divided into Southern Hemisphere Africa (SHAF), Arc of Deforestation (ARCD), South of the Arc of Deforestation (SARC), and Australia (AUST), according to the definitions described in van Marle et al.(17)

Figure S2. Trends of measured black carbon deposition fluxes compared with modeled values for co-located grid cells. Green and orange stacked contours represent contributions from biomass burning (BB4CMIP or LPJ-LMfire) and anthropogenic fossil fuel and biofuel emissions (CEDS), respectively. (a) Measured vs. modeled (BB4CMIP + CEDS) over Antarctica; (b) same as (a) but modeled with LPJ-LMfire + CEDS. Black curves in (a) and (b) represent the median values of 12 ice core records. Shaded grey areas in (a) and (b) represent the 25th to 75th percentile range across sites. (c) Measured vs. modeled (BB4CMIP + CEDS) over Bolivia Andes; (d) same as (c) but modeled with LPJ-LMfire + CEDS. The black curve in (b) represents the 30-year running average of black carbon ratios in an Andean ice core record from Illimani, Bolivia(22). Light grey curves in (c) and (d) represent the annually averaged ice core record.

Figure S3. Comparison between (a) the mean values of the z-scores of black carbon fluxes from 14 Antarctic ice cores and climate oscillation indices including (b) the ENSO index (NINO3), (c) Indian ocean dipole (IOD) mode index, and (d) Southern annular mode (SAM) index. The thin lines represent annual data, and the thick lines are 21-year moving average values. The correlation coefficients r between the annual data of BC flux z-score and NINO3, IOD and SAM indices are -0.08 ($p = 0.33$), 0.14 ($p = 0.10$), and 0.09 ($p = 0.50$), respectively. None of these correlations is statistically significant at the 0.05 level. Correlation coefficients for each individual ice core record can be found in Table S2.

Figure S4. Scatter plot (a) and colored map (b) compare present-day modeled versus measured annual mean BC deposition flux over Antarctica. The model simulations are performed for 1998-2002 with CEDS fossil fuel/biofuel emissions and GFED4 biomass burning emissions. Measured values are derived from ice core records for the mean of 1985-2010. Solid line in (a) is fit to the data; the dashed line is the 1:1 line. Small circles in (b) indicate observed BC fluxes, while background contours represent the model results.

Figure S5. Ratios between satellite-observed burned areas and burned areas modeled by LPJ-LMfire for the period from 1998 to 2015. These ratios are used as scaling factors to correct LPJ-LMfire biomass burning emissions in post-processing.

Figure S6. Hovmöller plots showing (a) cropland area and (b) pasture area in the Southern Hemisphere from 1700 to 2000 CE. Color represents zonal land use area in each 1-degree latitude band.

Figure S7. Modeled cloud condensation nuclei (CCN) number concentration for preindustrial (a) and the present day (b) simulated with CEDS fossil fuel/biofuel emissions and LPJ-LMfire biomass burning emissions. Ratios of CCN number concentrations simulated using two different biomass burning emission inventories with the same fossil fuel/biofuel emissions (LPJ-LMfire + CEDS to BB4CMIP + CEDS) are illustrated in (c) for 1750 and (d) for the 2000. CCN number concentrations are calculated for a supersaturation ratio of 0.2% at the level of 915 hPa, based on the size-resolved aerosol composition output from GEOS-Chem-TOMAS simulations.

Figure S8. Modeled cloud albedo effect as a function of hemispheric mean CCN number concentration. Data are shown for the Southern Hemisphere (SH, circles) and the Northern Hemisphere (NH, squares) separately. Each data point represents the 5-yr average of the simulated time slice between 1750 and 2000. The values are relative to the year of 2000. Fitted lines in grey are shown in the figure to guide the eye, with a solid line for the Southern Hemisphere and a dashed line for the Northern Hemisphere.

Figure S9. Scatter plot (a) and colored map (b) show the comparison of the present-day annual precipitation rates derived from MERRA2 reanalysis data and accumulation rates derived from ice cores over Antarctica. Solid line in (a) is fit to the data; the dashed line is the 1:1 line. Small circles in (b) indicate the modern-day accumulation rates derived from ice core annual layers. Background contours of the map in (b) represents the annual mean precipitation rates of 1998-2002 derived from MERRA2 dataset.

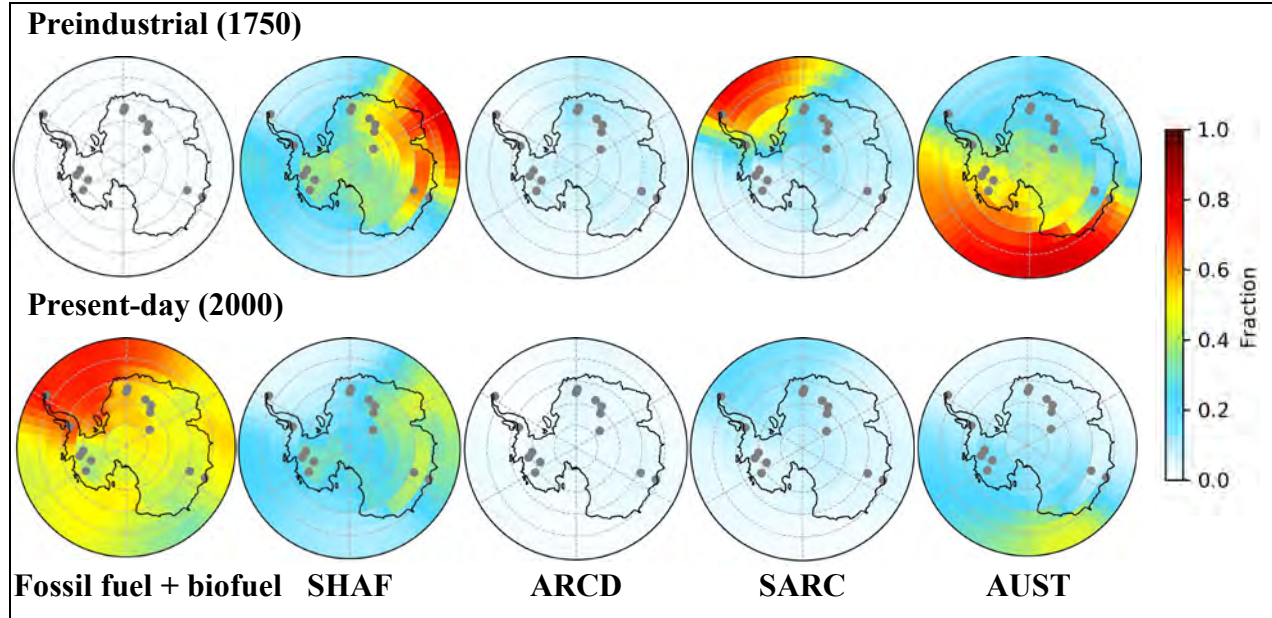


Figure S1. Modeled contributions of Antarctic BC deposition from anthropogenic fossil fuel/biofuel emissions and open biomass burning emissions from different regions in the Southern Hemisphere. The simulations are performed using GEOS-Chem-TOMAS with CEDS anthropogenic fossil fuel and biofuel emissions and LPJ-LMfire biomass burning emissions (see Methods). Gray dots represent the locations of ice core sites. The biomass burning regions in the Southern Hemisphere are divided into Southern Hemisphere Africa (SHAF), Arc of Deforestation (ARCD), South of the Arc of Deforestation (SARC), and Australia (AUST), according to the definitions described in van Marle et al.(17)

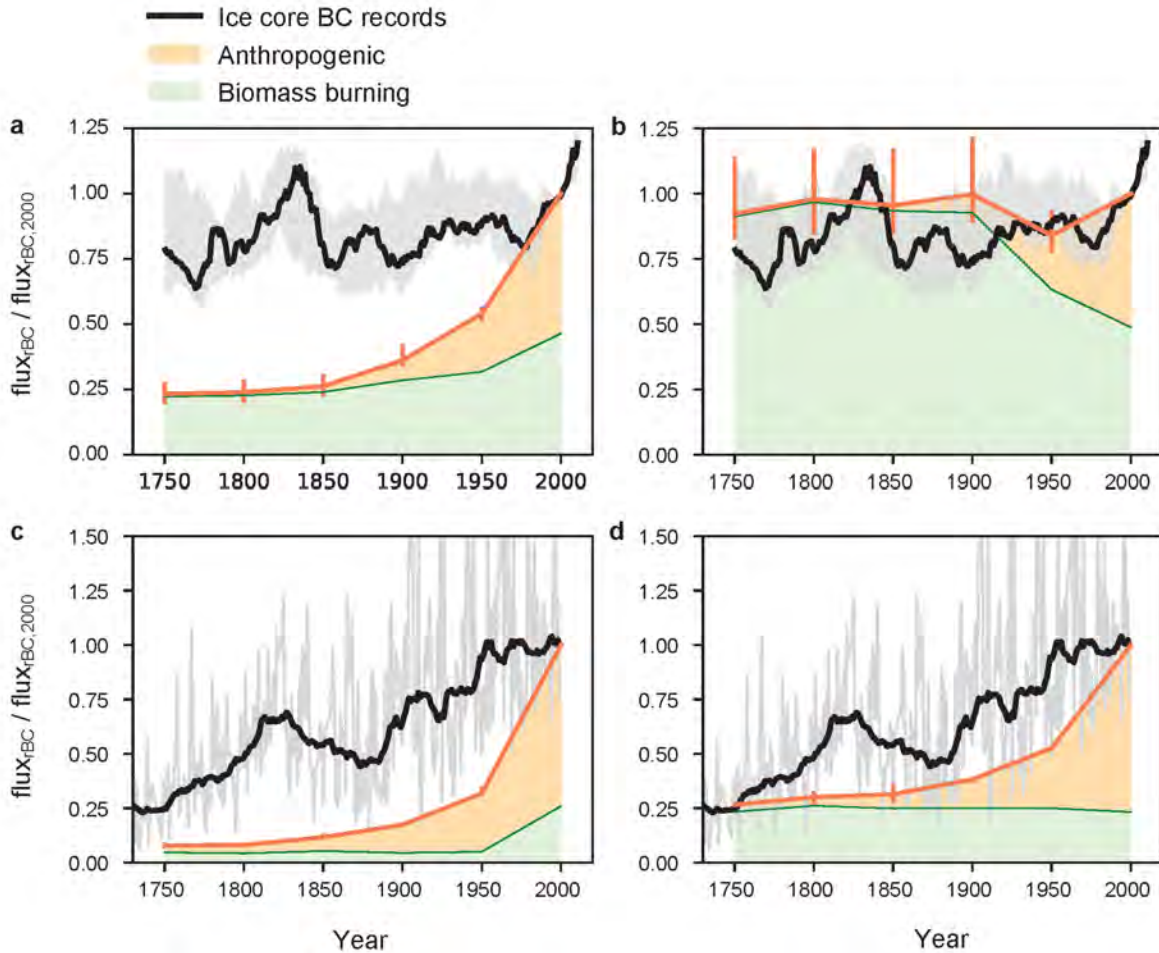


Figure S2. Trends of measured black carbon deposition fluxes compared with modeled values for co-located grid cells. Green and orange stacked contours represent contributions from biomass burning (BB4CMIP or LPJ-LMfire) and anthropogenic fossil fuel and biofuel emissions (CEDS), respectively. (a) Measured vs. modeled (BB4CMIP + CEDS) over Antarctica; (b) same as (a) but modeled with LPJ-LMfire + CEDS. Black curves in (a) and (b) represent the median values of 12 ice core records. Shaded grey areas in (a) and (b) represent the 25th to 75th percentile range across sites. (c) Measured vs. modeled (BB4CMIP + CEDS) over Bolivia Andes; (d) same as (c) but modeled with LPJ-LMfire + CEDS. The black curve in (b) represents the 30-year running average of black carbon ratios in an Andean ice core record from Illimani, Bolivia(22). Light grey curves in (c) and (d) represent the annually averaged ice core record.

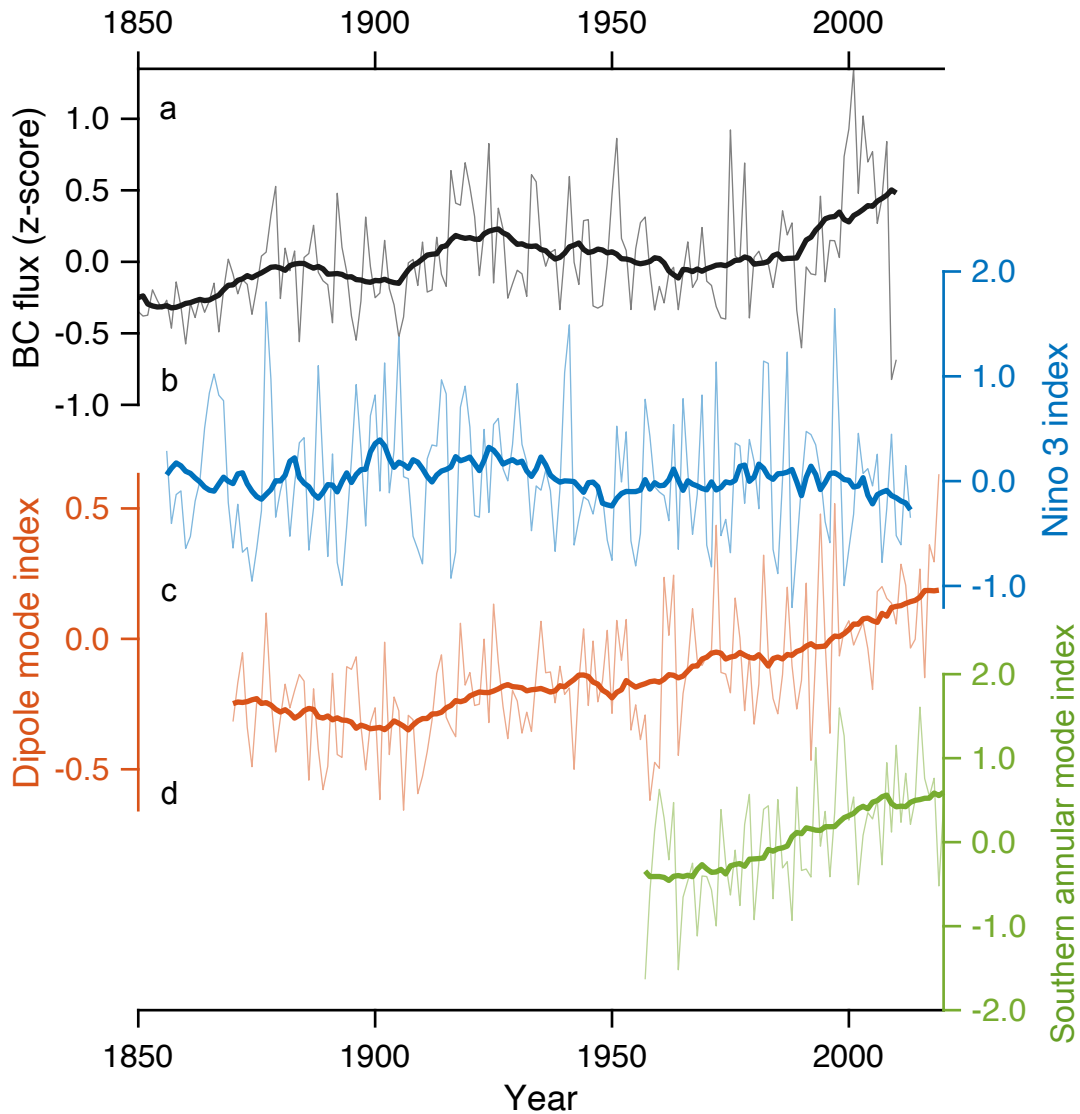


Figure S3. Comparison between (a) the mean values of the z-scores of black carbon fluxes from 14 Antarctic ice cores and climate oscillation indices including (b) the ENSO index (NINO3), (c) Indian ocean dipole (IOD) mode index, and (d) Southern annular mode (SAM) index. The thin lines represent annual data, and the thick lines are 21-year moving average values. The correlation coefficients r between the annual data of BC flux z-score and NINO3, IOD and SAM indices are -0.08 ($p = 0.33$), 0.14 ($p = 0.10$), and 0.09 ($p = 0.50$), respectively. None of these correlations is statistically significant at the 0.05 level. Correlation coefficients for each individual ice core record can be found in Table S2.

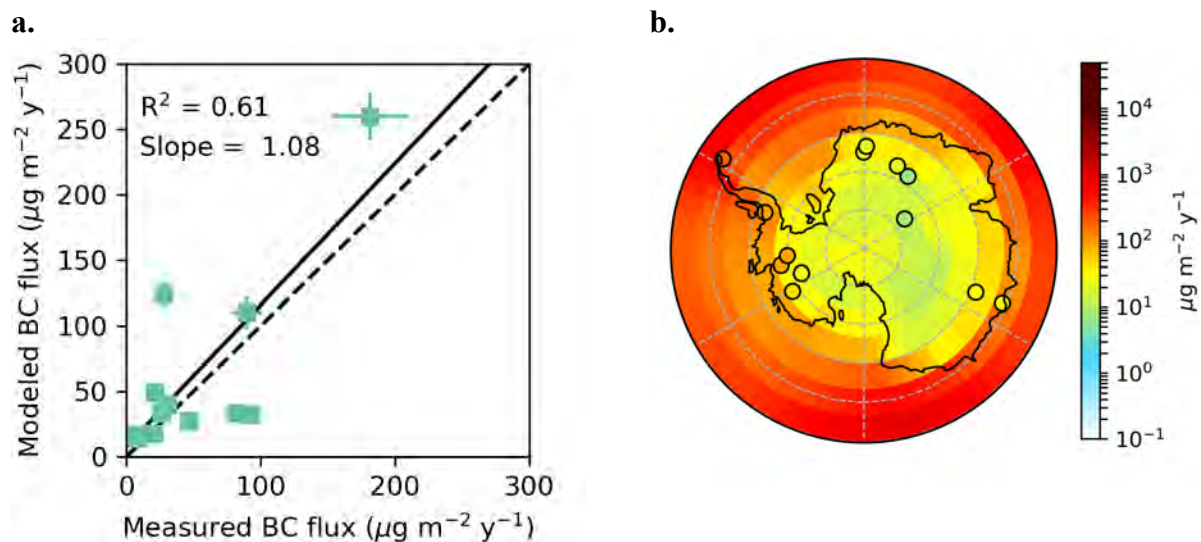


Figure S4. Scatter plot (a) and colored map (b) compare present-day modeled versus measured annual mean BC deposition flux over Antarctica. The model simulations are performed for 1998-2002 with CEDS fossil fuel/biofuel emissions and GFED4 biomass burning emissions. Measured values are derived from ice core records for the mean of 1985-2010. Solid line in (a) is fit to the data; the dashed line is the 1:1 line. Small circles in (b) indicate observed BC fluxes, while background contours represent the model results.

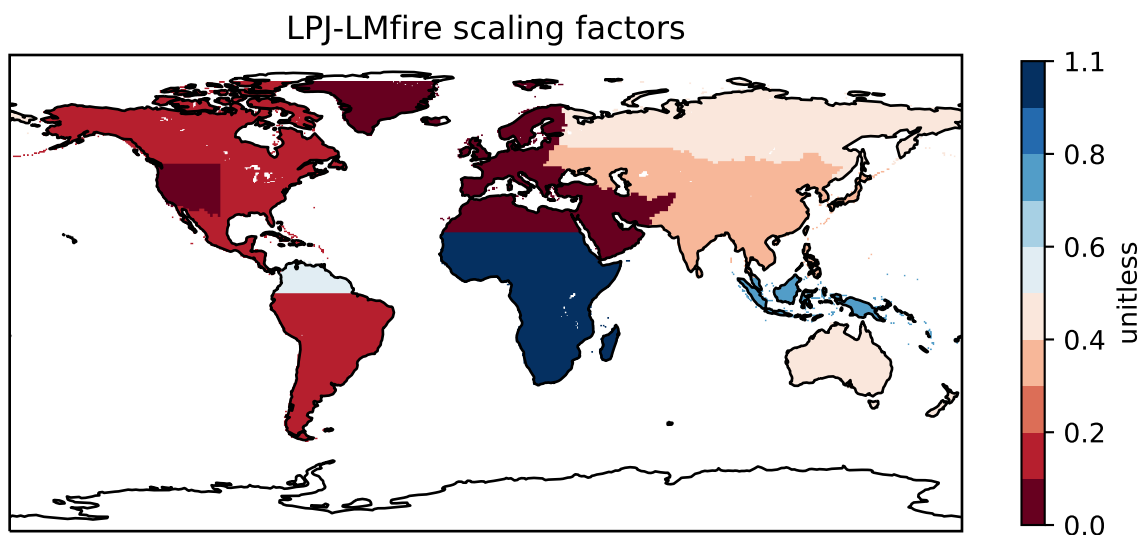


Figure S5. Ratios between satellite-observed burned areas and burned areas modeled by LPJ-LMfire for the period from 1998 to 2015. These ratios are used as scaling factors to correct LPJ-LMfire biomass burning emissions in post-processing.

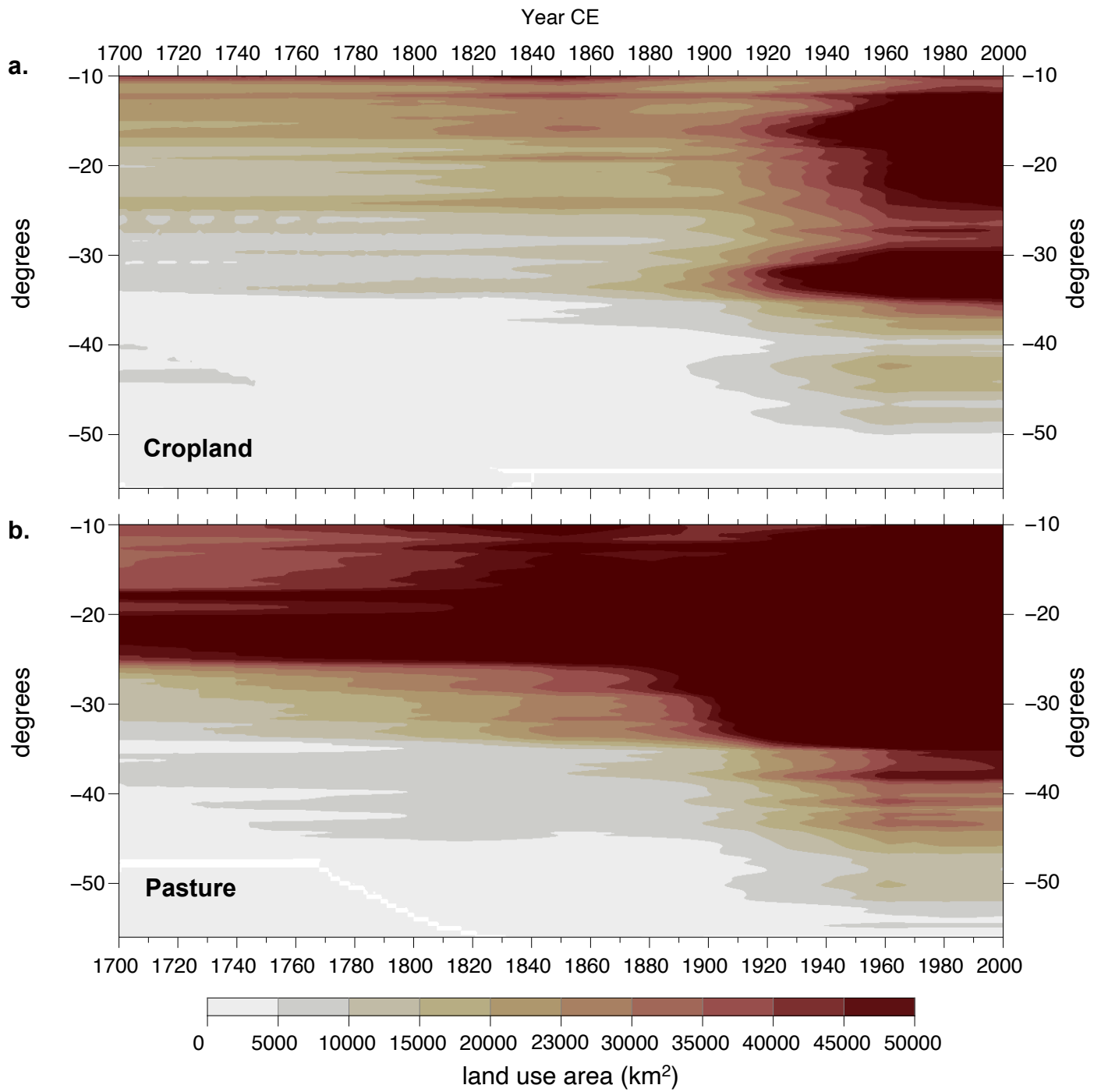


Figure S6. Hovmöller plots showing (a) cropland area and (b) pasture area in the Southern Hemisphere from 1700 to 2000 CE. Color represents zonal land use area in each 1-degree latitude band.

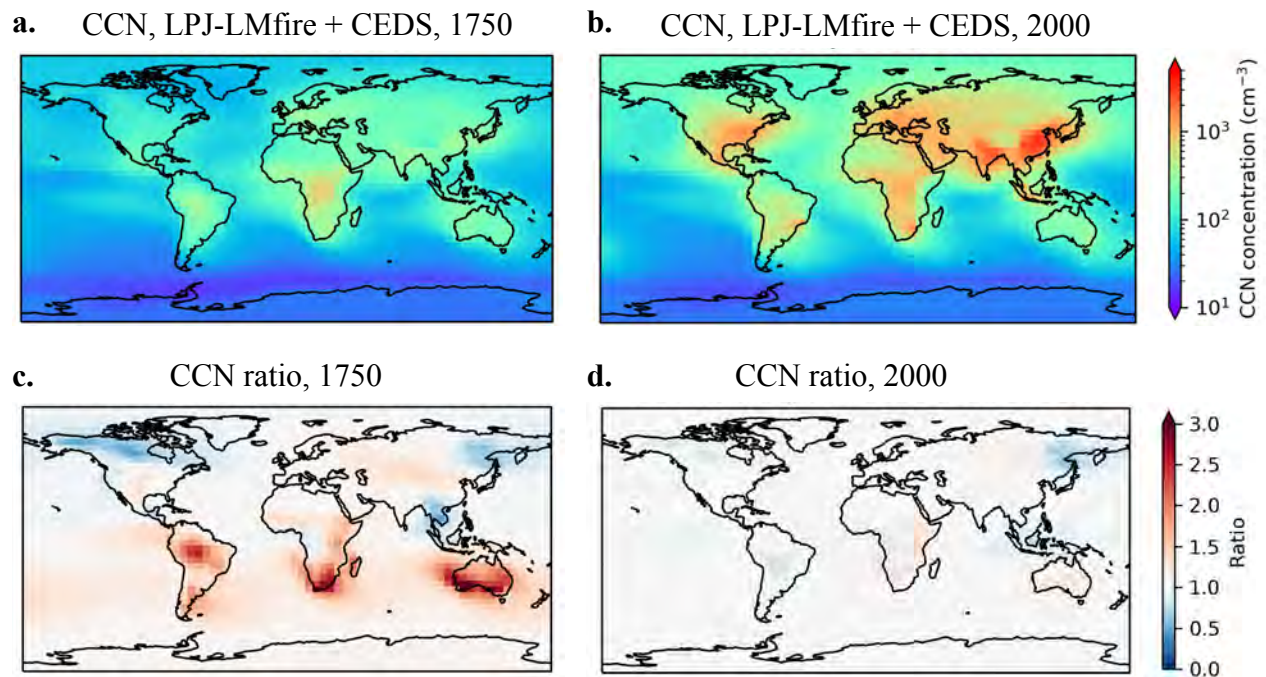


Figure S7. Modeled cloud condensation nuclei (CCN) number concentration for preindustrial (a) and the present day (b) simulated with CEDS fossil fuel/biofuel emissions and LPJ-LMfire biomass burning emissions. Ratios of CCN number concentrations simulated using two different biomass burning emission inventories with the same fossil fuel/biofuel emissions (LPJ-LMfire + CEDS to BB4CMIP + CEDS) are illustrated in (c) for 1750 and (d) for the 2000. CCN number concentrations are calculated for a supersaturation ratio of 0.2% at the level of 915 hPa, based on the size-resolved aerosol composition output from GEOS-Chem-TOMAS simulations.

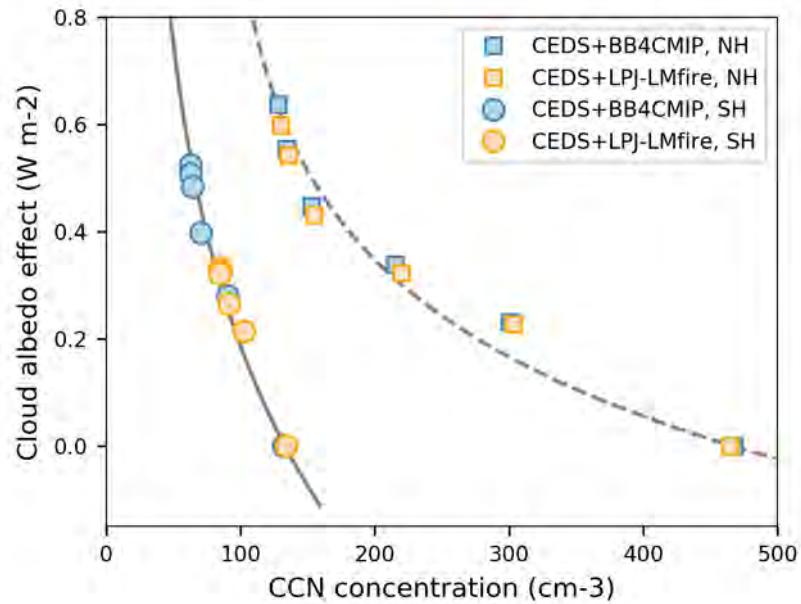


Figure S8. Modeled cloud albedo effect as a function of hemispheric mean CCN number concentration. Data are shown for the Southern Hemisphere (SH, circles) and the Northern Hemisphere (NH, squares) separately. Each data point represents the 5-yr average of the simulated time slice between 1750 and 2000. The values are relative to the year of 2000. Fitted lines in grey are shown in the figure to guide the eye, with a solid line for the Southern Hemisphere and a dashed line for the Northern Hemisphere.

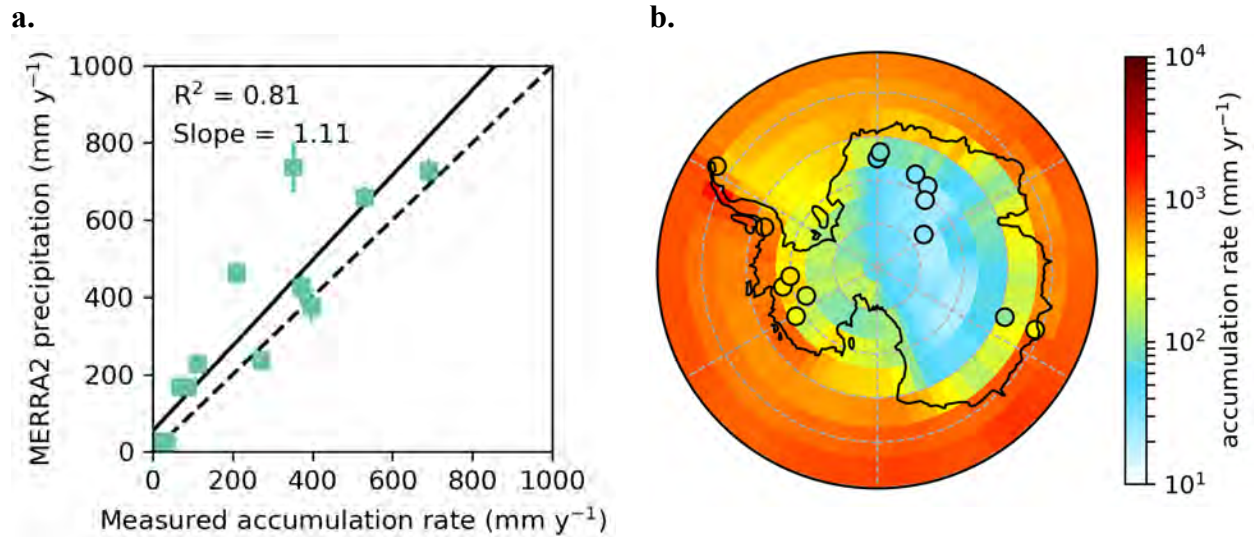


Figure S9. Scatter plot (a) and colored map (b) show the comparison of the present-day annual precipitation rates derived from MERRA2 reanalysis data and accumulation rates derived from ice cores over Antarctica. Solid line in (a) is fit to the data; the dashed line is the 1:1 line. Small circles in (b) indicate the modern-day accumulation rates derived from ice core annual layers. Background contours of the map in (b) represents the annual mean precipitation rates of 1998-2002 derived from MERRA2 dataset.